

Physics-informed Neural Networks for Heterogeneous Poroelastic Media

Sumanta Roy^a, Chandrasekhar Annavarapu^{a,*}, Pratanu Roy^b, Dakshina Murthy Valiveti^c

^a*Department of Civil Engineering, Indian Institute of Technology Madras, Chennai, 600036, Tamil Nadu, India*

^b*Atmospheric, Earth and Energy Division, Lawrence Livermore National Laboratory, Livermore, 94551, California, United States*

^c*Engineering and Computational Physics, Energy Sciences and Research, ExxonMobil Technology and Engineering, Spring, 77389, Texas, United States*

Abstract

This study introduces a novel physics-informed neural networks (PINNs) framework designed to model coupled-field problems specifically tailored for heterogeneous poroelastic media. Firstly, a composite neural network is developed where distinct neural networks are dedicated to predicting displacement and pressure variables for each material, employing identical activation functions but trained separately across all other parameters. Secondly, we handle the challenges of heterogeneous material interfaces by the Interface-PINNs (I-PINNs) framework, where different activation functions across any material interface are prescribed to ensure that the discontinuities in solution fields and gradients are accurately captured. We compare the modified PINNs framework with the conventional approach on two one-dimensional benchmark examples for poroelasticity in heterogeneous media. Furthermore, we assess a single neural network architecture, comparing it against the composite neural network proposed in this work. These examples show that the proposed framework demonstrates superior approximation accuracy in both displacements and pressures, and better convergence behavior.

Keywords: Physics-informed neural networks, scientific machine learning, deep learning, interface problems, poromechanics, coupled problems

*Corresponding author

Email address: annavarapuc@civil.iitm.ac.in (Chandrasekhar Annavarapu)

1. Introduction

Various geothermal and subsurface energy applications are governed by the dynamics of fluid flow within poroelastic media. This encompasses activities like hydrocarbon retrieval from oil and gas reservoirs [1], geological storage of carbon dioxide [2], and harnessing energy from subsurface thermal systems [3]. In reservoir engineering [4, 5], these interactions are key in determining the state of subsurface fluids and gases, the performance of production wells, and the deformation of the porous subsurface media. In geothermal systems, heat below the ground is transported to the surface through fluid flow, requiring a thorough thermo-hydro-poromechanical analysis for system optimization. Furthermore, the inherent heterogeneity characterizing these subsurface systems adds a layer of complexity. Heterogeneities may stem from the natural stratification of the earth’s crust, the presence of naturally occurring faults, or induced variations due to processes such as hydraulic fracturing [6]. The diverse nature of these systems can significantly affect the behavior and movement of fluids below the surface. Therefore, a thorough investigation and comprehension of subsurface heterogeneity, coupled with the intricate thermo-hydro-poromechanical processes, emerge as imperative aspects of studying geothermal and subsurface applications.

Computational modeling is often necessary to supplement theoretical and experimental investigations to gain fundamental insight into the coupled physical processes of flow and deformation. On the one hand, compared to a fully theoretical investigation, a computational model can relax simplifying assumptions on problem geometry, presence of material interfaces, and defects. On the other hand, compared to an experimental study, computational models are relatively inexpensive and provide a virtual laboratory to conduct numerical experiments at a fraction of the cost.

Computational models of these thermo-hydro-poromechanical systems can be broadly categorized as either physics-based or data-driven. Physics-based models involve the solution of coupled partial differential equations (PDEs). These coupled PDEs are solved numerically, often employing methods like the finite element method [7, 8, 9, 10], finite volume method [11], or finite difference method [12], that provide approximate solutions to the PDEs on an underlying grid. However, generating grids that conform to subsurface features (such as material interfaces, faults, and fractures) is a time-

consuming pre-processing step. For instance, in several reservoir engineering applications, the cost of grid generation is comparable to (or exceeds) the cost of analysis [13, 14, 15]. This makes computational modeling intractable for realistic field-scale applications. By contrast, data-driven models employ machine learning (ML), particularly artificial neural networks (ANNs), to predict the coupled behavior. However, their accuracy relies on the availability and quality of training data, which can be sparse in subsurface systems due to economic constraints. As such, the applicability of purely data-driven models in poroelasticity is also severely limited.

Physics-informed neural networks (PINNs), a recently developed hybrid approach [16], combines aspects of both physics-based and data-driven modeling. On the one hand, PINNs are not grid-based and thereby eliminate the need for conforming meshes. On the other hand, PINNs leverage fundamental physical laws including governing PDEs, initial and boundary conditions, and data, to construct a loss functional and thereby do not require extensive training datasets. PINNs approximate unknown field variables using feed-forward neural networks to minimize the loss functionals constructed from governing PDEs, initial and boundary conditions at randomly selected collocation points across the domain. PINNs have been successfully applied to solve problems in various domains, including solid mechanics [17, 18], fluid mechanics [19, 20], heat transfer [21, 22], inverse problems [23, 24] to name a few.

In the context of this study, it is crucial to note that, at present, the thermal effects were specifically excluded, directing the attention solely to a 1D coupled hydro-poromechanical analysis. However, it is important to highlight that the framework can be easily extended to model multi-physics processes by incorporating thermal behavior, thus enabling a comprehensive solution for a completely coupled thermo-hydro-poromechanical analysis. Although PINNs were explored as forward solvers to model poroelasticity [25, 26], those were limited to homogeneous materials with only a loose coupling between the governing equations describing solid deformation and fluid flow. The objectives of this study were, therefore, two-fold. Firstly, a modified PINNs architecture capable of modeling poroelastic response for multilayered media characterized by material property discontinuities at interfaces was proposed. Secondly, through several numerical examples in 1D, it was demonstrated that composite neural network architectures are advantageous compared to single neural networks for coupled-field problems. The practical applicability of this framework extends to serving as a numerical solver

for interface problems, proving particularly useful in modeling heterogeneous subsurface and geothermal systems with numerous material interfaces due to the presence of geological stratification and numerous faults.

The rest of the paper is organized as follows: Section 2 outlines the governing differential equations for poroelasticity in a heterogeneous domain. Section 3 provides an overview of PINNs, followed by a detailed description of the proposed PINNs architecture tailored for handling poroelasticity in heterogeneous materials. Here, the architecture of the proposed PINNs framework for heterogeneous poroelasticity is described, along with its implementation, and guidelines for improving accuracy and convergence are provided. In Section 4, the numerical results of the proposed PINNs architecture are compared with those obtained using the conventional PINNs approach. The evaluation encompasses numerical accuracy and computational costs on two specific 1D heterogeneous poroelastic problems. Following this analysis, a sensitivity assessment is conducted, wherein the performance of the proposed framework for each applied modification is evaluated. Finally, Section 5 presents concluding remarks and provides an outlook for the work.

2. Governing Equations

The mechanical behavior of a porous medium is influenced by the presence of a moving fluid within it. Simultaneously, alterations in the mechanical state of the porous structure impact the fluid’s conduct within the pores. The foundational principles of poroelasticity revolve around the interconnected phenomena of deformation and diffusion: fluid-to-solid coupling takes place when variations in fluid pressure or mass result in the deformation of the porous framework, while solid-to-fluid coupling occurs when changes in the stress of the porous structure lead to adjustments in fluid pressure or mass. In line with these phenomena, the time-dependent nature of the fluid-filled porous medium becomes apparent. Suppose the porous medium undergoes compression, leading to an increase in fluid pressure within the pores and subsequent fluid flow. The temporal evolution of fluid pressure, characterized by the dissipation of pressure through diffusive fluid flux according to Darcy’s law, initiates a time-dependent modification in poroelastic stresses. These stresses, in turn, reciprocate by influencing the fluid pressure field. Evidently, the model depicting this process is time-dependent and can be considered quasi-static when inertial forces are neglected.

The governing equations have been formulated under the assumptions of quasi-static, linearized poroelasticity [27] such that in a one-dimensional bounded domain $\Omega = [0, L]$, partitioned into two non-overlapping sub-domains $\Omega_1 = [0, \zeta]$ and $\Omega_2 = [\zeta, L]$ by a perfectly bonded material interface at $x = \zeta \in (0, L)$ such that $\Omega = \Omega_1 \cup \Omega_2$. The displacements $u_m(x, t)$ and pressures $p_m(x, t)$ that satisfy the following equations simultaneously in each subdomain Ω_m (for $m = 1, 2$) are sought:

$$\frac{\partial}{\partial x} \left((\lambda_m + 2\mu_m) \frac{\partial u_m}{\partial x} \right) + \alpha \frac{\partial p_m}{\partial x} = h_m(x, t), x \in \Omega_m, 0 < t \leq T, \quad (1)$$

$$\frac{\partial}{\partial t} \left(\phi_m \beta_m p_m + \frac{\partial u_m}{\partial x} \right) - \frac{\partial}{\partial x} \left(\frac{\kappa_m}{\eta_m} \frac{\partial p_m}{\partial x} \right) = q_m(x, t), x \in \Omega_m, 0 < t \leq T, \quad (2)$$

where, for each subdomain Ω_m , λ_m, μ_m are the Lamé's parameters; $\alpha, \phi_m, \beta_m, \kappa_m$, and η_m denote the Biot-Willis constant, porosity, fluid compressibility, intrinsic permeability, and fluid viscosity, respectively. Additionally, $q_m(x, t)$ is the volumetric source/sink term, and $h_m(x, t)$ is the external body force on the medium (both of which are taken to be zero). The quantities denoted by a subscript m can be discontinuous across the interface. Figure 1 shows the schematic of the problem domain containing a poroelastic media with one interface. The boundary and initial conditions are given as:

$$(\lambda_1 + 2\mu_1) \frac{\partial u_1}{\partial x} = -s_0 \text{ at } x = 0 \text{ and } u_2 = 0 \text{ at } x = L, \quad (3a)$$

$$p_1 = 0 \text{ at } x = 0 \text{ and } \frac{\partial p_2}{\partial x} = 0 \text{ at } x = L, \quad (3b)$$

$$\phi_m \beta_m p_m + \frac{\partial u_m}{\partial x} = 0, \text{ for } x \in \Omega, t = 0. \quad (3c)$$

The applied load on $x = 0$ is given as s_0 . The initial condition assumes a zero initial change in water content. To make the data suitable for deep learning frameworks, quantities were non-dimensionalized by employing the characteristic length L and reference values of Lamé's coefficients, permeability, and viscosity. This is achieved through the following variable substitution:

$$x := \frac{x}{L}, \quad t := \frac{(\lambda_0 + 2\mu_0)\kappa_0 t}{\eta L^2}, \quad u_m := \frac{(\lambda_0 + 2\mu_0)u_m}{s_0 L}, \quad p_m := \frac{p_m}{s_0}, \quad \nu_m := \frac{\lambda + 2\mu}{\lambda_0 + 2\mu_0},$$

$$\kappa_m := \frac{\kappa_m/\eta_m}{\kappa_0/\eta_0}, \quad a_m := \phi_m \beta_m (\lambda_0 + 2\mu_0), \quad f_m(x, t) := \frac{\eta_0 L^2}{s_0 \kappa_0} q_m(x, t).$$

Here, the quantities with subscript ‘0’ designates reference values for the associated parameters. Additionally, homogeneous boundary conditions are established using the substitution $u_m(x, t) := u_m(x, t) + x - 1$. Consequently, the resulting nondimensionalized system becomes:

$$-\frac{\partial}{\partial x} \left(\nu_m \frac{\partial u_m}{\partial x} \right) + \frac{\partial p_m}{\partial x} = 0, x \in \Omega_m, 0 < t \leq T, \quad (4)$$

$$\frac{\partial}{\partial t} \left(a_m p_m + \frac{\partial u_m}{\partial x} \right) - \frac{\partial}{\partial x} \left(\kappa_m \frac{\partial p_m}{\partial x} \right) = f_m(x, t), x \in \Omega_m, 0 < t \leq T, \quad (5)$$

with the boundary and initial conditions:

$$\nu_1 \frac{\partial u_1}{\partial x} = 0 \text{ at } x = 0 \text{ and } u_2 = 0 \text{ at } x = 1, \quad (6a)$$

$$p_1 = 0 \text{ at } x = 0 \text{ and } \kappa_2 \frac{\partial p_2}{\partial x} = 0 \text{ at } x = 1, \quad (6b)$$

$$a_m p_m + \frac{\partial u_m}{\partial x} = 1, \text{ for } x \in \Omega, t = 0. \quad (6c)$$

The interface conditions (at $x = \zeta$) ensure the continuity of fluxes and the primary variables at the interface such that

$$\llbracket u \rrbracket = 0, \quad \left[\left[\nu \frac{\partial u}{\partial x} \right] \right] = 0, \quad \llbracket p \rrbracket = 0, \quad \left[\left[\kappa \frac{\partial p}{\partial x} \right] \right] = 0. \quad (7)$$

The operator $\llbracket \odot \rrbracket = \odot_2 - \odot_1$ represents a jump in the field \odot . The coefficients are piecewise constant across the interface, as follows:

$$\nu(x) = \begin{cases} \nu_1, & x \leq \zeta \\ \nu_2, & x > \zeta \end{cases}, \quad a(x) = \begin{cases} a_1, & x \leq \zeta \\ a_2, & x > \zeta \end{cases}, \quad \kappa(x) = \begin{cases} \kappa_1, & x \leq \zeta \\ \kappa_2, & x > \zeta \end{cases}. \quad (8)$$

3. Physics-informed Neural Networks for Heterogeneous Poroelastic Media

3.1. Physics-informed Neural Networks

Over the last few decades, significant efforts have been devoted to leveraging ML approaches, such as support vector machines [28, 29], Gaussian processes [30, 31] and artificial neural networks [32, 33, 34, 35] to model physical processes. Many of these approaches operate as data-driven mechanisms,

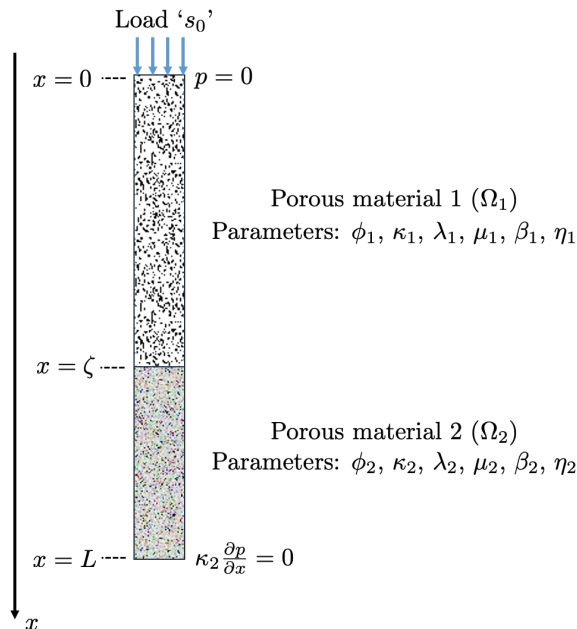


Figure 1: Problem domain in one dimension: The bottom surface is fixed, while the top surface is subjected to stress s_0 ; no-flux boundary condition is imposed on the bottom surface, while a zero-pressure condition is imposed on the top.

treating ML as a black-box tool. However, the accuracy of these approximations is heavily reliant on the quality and quantity of the training data employed. This poses a substantial challenge in engineering applications, where issues like data accessibility, validity, noise, and various uncertainties come into play. Furthermore, there is no assurance that the ML models faithfully capture the underlying physics of the problem. A constructive solution to these challenges has emerged through the innovative application of PINNs. PINNs use deep neural networks (DNNs) to approximate solutions to the governing differential equations (ODEs/PDEs). DNNs are structured like the human brain, with interconnected hidden layers containing nodes called neurons. These models integrate the physics of the problem as soft constraints guiding the optimization process. The loss functional $\mathcal{L}(\theta)$ consists of the linear combination of the residual of PDEs, interface, boundary, and initial conditions. The goal is to minimize $\mathcal{L}(\theta)$ by optimizing the parameter set θ on randomly selected collocation points within the domain and on boundaries.

Consider the time-varying PDE $\mathcal{P}u(x, t) = f(x, t)$, where \mathcal{P} represents

the differential operator, and $f(x, t)$ is the source function. The dependent variable $u(x, t)$ is defined on the domain $\Omega \times T$, with $\Omega \in \mathcal{R}^d$ and $T \in \mathcal{R}$ representing the spatial and temporal domains respectively. The real space and number of dimensions in the real space are denoted by \mathcal{R} and d respectively. The PDE is subjected to Dirichlet boundary condition $b_D(x, t)$ on Γ_D , Neumann boundary condition $b_N(x, t)$ on Γ_N , such that, $\Gamma_D \cup \Gamma_N = \partial\Omega$, where $\partial\Omega$ denotes the entire boundary of the computational domain Ω . It is also subjected to the initial condition $u_0(x)$ at $t = 0$. According to PINNs, the unknown variable $u(x, t)$ is approximated by a DNN $u(x, t) \approx \tilde{u} = \mathcal{N}(x, t, \theta)$. The flux at boundary $\tilde{q} = \nabla \tilde{u} \cdot \mathbf{n}$, as well as the PDE residual $\mathcal{P}u(x, t) - f(x, t)$ is computed using the automatic differentiation (AD) technique [36]. The normal to the boundary is denoted by \mathbf{n} . Therefore, the total loss functional is defined as

$$\begin{aligned} \mathcal{L} = & \lambda_1 \|\mathcal{P}\tilde{u}(x, t) - f(x, t)\|_{\Omega \times T} \\ & + \lambda_2 \|\tilde{u}(x, t) - b_D\|_{\Gamma_D \times T} \\ & + \lambda_3 \|\tilde{q}(x, t) - b_N\|_{\Gamma_N \times T} \\ & + \lambda_4 \|\tilde{u}(x, t) - u_0\|_{\Gamma_D \times t=0} \end{aligned} \quad (9)$$

In Eq. (9), the quantity $\|\odot\|$ represents an error metric, and the term λ_i represents the penalty (weight) associated with i -th loss term. Two common error metrics are mean square errors (MSE) and sum of square errors (SSE). The loss functional is minimized over a set of collocation points sampled across the spatiotemporal domain $\Omega \times T$, the boundary $\partial\Omega \times T$, and at the initial condition $\Omega \times t = 0$.

As described before, the approximation $\tilde{u}(x, t)$ is obtained using a DNN, which is essentially a feed-forward network consisting of a collection of neurons arranged in consecutive layers. Neurons in adjacent layers of the fully connected network are linked, whereas neurons within one single layer are not connected. For a deep neural network with K layers consisting of an input layer, an output layer, and $K - 2$ hidden layers, the network approximation can be represented as a combination of K mathematical functions $\mathcal{A}_i(\mathbf{x}_i, \theta_i)$ as follows:

$$\tilde{u} = \mathcal{N}(x, t, \theta) = \mathcal{A}_K \circ \mathcal{A}_{K-1} \circ \mathcal{A}_{K-2} \cdots \circ \mathcal{A}_1(x, t) \quad (10)$$

The layer composition \circ is to be read as $\mathcal{A}_2(\mathcal{A}_1(\mathbf{x}, \theta))$. The function \mathcal{A} can be a linear or non-linear function such that

$$\mathcal{A}_i(\mathbf{x}_i, \theta_i) = \sigma(\mathbf{w}_i^T \mathbf{x}_i + \mathbf{b}_i) \quad (11)$$

where, σ is known as the activation function, \mathbf{x}_i is the input vector to the i -th layer, and θ_i denotes the set of parameters for the i -th layer consisting of the weight matrix (\mathbf{w}_i) and bias vector (\mathbf{b}_i). A schematic of PINNs is shown in Figure 2(a).

3.2. Interface PINNs (I-PINNs)

It is important to highlight that Eqs. (5), (6c), (7), and (8) may result in solutions with weak (slope) discontinuities. The conventional PINNs architecture, however, is not effective in handling discontinuous solution fields. As noted in previous studies [37, 38], the traditional neural network architecture tends to produce uniform and continuous approximations throughout the domain, thereby failing to capture jumps (or kinks) at interfaces. Here, a modified PINNs framework termed Interface-PINNs (I-PINNs) is utilized. This framework was introduced previously by Sarma et al. [39, 40] due to its superior accuracy and convergence compared to conventional PINNs and other domain-decomposition-based PINNs (like M-PINN [41] and XPINNs [42]) for interface problems. In I-PINNs, the domain is decomposed into homogeneous sub-domains, and separate neural networks are employed for each sub-domain. These networks share parameters while using distinct activation functions, as illustrated in Figure 2(b). Interface conditions, as described by Eq. (7), are incorporated as additional terms in the loss functional. Notably, the neural networks across the interface communicate through a shared set of parameters and interface conditions. Simultaneously, the use of different activation functions on either side of the interface allows for flexibility in approximating discontinuities at the interface. An improved version of I-PINNs, termed Adaptive I-PINNs (AdaI-PINNs), was developed by Roy et al. [43]. This version further enhances the computational efficiency of I-PINNs, particularly for materials with multiple interfaces. However, in this study, we have restricted our usage to the original I-PINNs framework, as the numerical examples outlined here involve materials with only one interface.

3.3. I-PINNs for Coupled PDEs

As described in Section 2, the equations of poroelasticity in heterogeneous media require the solution of displacements, u_m , and pressures, p_m , in each subdomain, Ω_m . As such the I-PINNs framework must be appropriately modified for such coupled-field problems. A composite neural network (CoNN) framework is proposed, featuring distinct neural networks for each

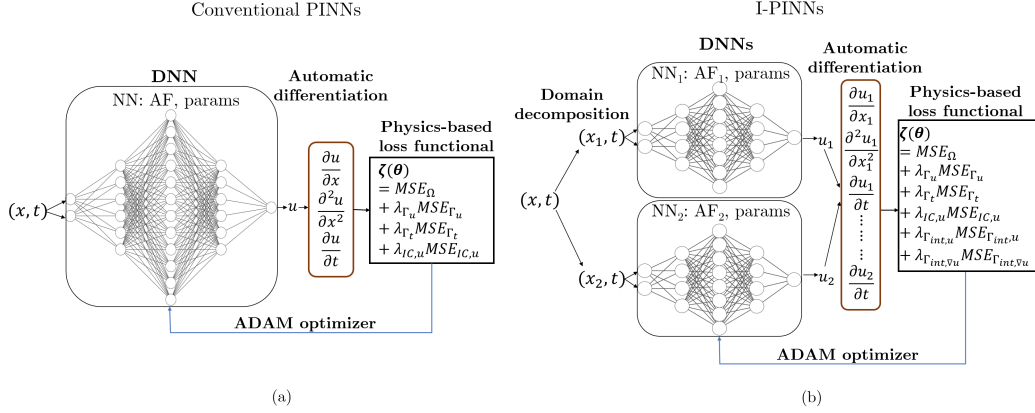


Figure 2: Schematic of (a) a conventional PINNs model, (b) I-PINNs for a problem in 1-D domain with two distinct regions divided by an interface. This modified setup involves the partitioning of input variables within these distinct domains, subsequently inputting them into separate neural networks utilizing different activation functions.

output field variable (i.e., displacements and pressures) within each subdomain. These neural networks have the same activation functions but different sets of parameters. However, to address discontinuities at material interfaces, this architecture is combined with the I-PINNs framework. In this combined approach, neural networks for distinct sub-domains share the same set of parameters but utilize different activation functions. As such, every output field variable gets a neural network with the same set of parameters throughout the problem domain, but with differing sets of activation functions across any material interface. However, the parameter set used in the neural networks is different for every output field variable. Figure 3 presents a schematic of the proposed architecture.

The architecture proposed in Figure 3 is to be contrasted with a straightforward extension of the I-PINNs architecture to poroelasticity problems in heterogeneous media where a single neural network (SNN) would feature two output neurons within each subdomain, each dedicated to representing a specific output field. While these neural networks would share the same set of parameters, they would employ different activation functions across a material interface, as in Figure 4.

Regardless of the type of architecture used (SNN or CoNN), the total loss functional aggregates mean square errors (MSEs) from various terms, including governing PDEs (linear momentum and mass balance equations summed

together as MSE_Ω), Dirichlet and Neumann boundary conditions for linear momentum balance (MSE_{Γ_u} and MSE_{Γ_t}), and mass balance (MSE_{Γ_p} , and MSE_{Γ_f}), the initial conditions for displacements ($\text{MSE}_{IC,u}$), and pressures ($\text{MSE}_{IC,p}$), and the interface compatibility conditions for displacements, tractions, pressures, and fluxes ($\text{MSE}_{\Gamma_{int,u}}$, $\text{MSE}_{\Gamma_{int,\sigma}}$, $\text{MSE}_{\Gamma_{int,p}}$, and $\text{MSE}_{\Gamma_{int,q}}$ respectively). This is represented as:

$$\begin{aligned} \mathcal{L}(\theta) = & \lambda_\Omega \text{MSE}_\Omega + \lambda_{\Gamma_u} \text{MSE}_{\Gamma_u} + \lambda_{\Gamma_t} \text{MSE}_{\Gamma_t} + \lambda_{\Gamma_p} \text{MSE}_{\Gamma_p} + \lambda_{\Gamma_f} \text{MSE}_{\Gamma_f} + \lambda_{IC,u} \text{MSE}_{IC,u} \\ & + \lambda_{IC,p} \text{MSE}_{IC,p} + \lambda_{\Gamma_{int,u}} \text{MSE}_{\Gamma_{int,u}} + \lambda_{\Gamma_{int,\sigma}} \text{MSE}_{\Gamma_{int,\sigma}} + \lambda_{\Gamma_{int,p}} \text{MSE}_{\Gamma_{int,p}} + \\ & \lambda_{\Gamma_{int,q}} \text{MSE}_{\Gamma_{int,q}} \quad (12) \end{aligned}$$

$$\text{MSE}_\Omega = \frac{1}{N_{\Omega \times T}} \left(\begin{array}{l} \sum_{i=1}^{N_{\Omega \times T}} \left[-\frac{\partial}{\partial x} \left(\nu \frac{\partial \tilde{u}}{\partial x} \right) + \frac{\partial \tilde{p}}{\partial x} \right] \\ + \sum_{i=1}^{N_{\Omega \times T}} \left[\frac{\partial}{\partial t} \left(a \tilde{p} + \frac{\partial \tilde{u}}{\partial x} \right) - \frac{\partial}{\partial x} \left(\kappa \frac{\partial \tilde{p}}{\partial x} \right) - f_m(x, t) \right] \end{array} \right) \quad (13a)$$

$$\text{MSE}_{\Gamma_u} = \frac{1}{N_{\Gamma_u}} \left(\sum_{i=1}^{N_{\Gamma_u}} [\tilde{u} - \dot{u}_D] \right) \quad (13b)$$

$$\text{MSE}_{\Gamma_t} = \frac{1}{N_{\Gamma_t}} \left(\sum_{i=1}^{N_{\Gamma_t}} \left[\nu \frac{\partial \tilde{u}}{\partial x} - \dot{u}_N \right] \right) \quad (13c)$$

$$\text{MSE}_{\Gamma_p} = \frac{1}{N_{\Gamma_p}} \left(\sum_{i=1}^{N_{\Gamma_p}} [\tilde{p} - \dot{p}_D] \right) \quad (13d)$$

$$\text{MSE}_{\Gamma_f} = \frac{1}{N_{\Gamma_f}} \left(\sum_{i=1}^{N_{\Gamma_f}} \left[\kappa \frac{\partial \tilde{p}}{\partial x} - \dot{p}_N \right] \right) \quad (13e)$$

$$\text{MSE}_{\Gamma_{IC}} = \frac{1}{N_{\Gamma_{IC}}} \left(\sum_{i=1}^{N_{\Gamma_{IC}}} [\tilde{u} - \dot{u}_{IC}] \right) \quad (13f)$$

$$\text{MSE}_{\Gamma_{IC}} = \frac{1}{N_{\Gamma_{IC}}} \left(\sum_{i=1}^{N_{\Gamma_{IC}}} [\tilde{p} - \dot{p}_{IC}] \right) \quad (13g)$$

$$\text{MSE}_{\Gamma_{int}} = \frac{1}{N_{\Gamma_{int}}} \left(\sum_{i=1}^{N_{\Gamma_{int}}} [[\tilde{u}]] \right) \quad (13h)$$

$$\text{MSE}_{\Gamma_{int}} = \frac{1}{N_{\Gamma_{int}}} \left(\sum_{i=1}^{N_{\Gamma_{int}}} \left[\left[\nu \frac{\partial \tilde{u}}{\partial x} \right] \right] \right) \quad (13i)$$

$$\text{MSE}_{\Gamma_{int}} = \frac{1}{N_{\Gamma_{int}}} \left(\sum_{i=1}^{N_{\Gamma_{int}}} \llbracket \tilde{p} \rrbracket \right) \quad (13j)$$

$$\text{MSE}_{\Gamma_{int}} = \frac{1}{N_{\Gamma_{int}}} \left(\sum_{i=1}^{N_{\Gamma_{int}}} \left[\left[\kappa \frac{\partial \tilde{p}}{\partial x} \right] \right] \right) \quad (13k)$$

$N_{\Omega \times T}$ is the number of collocation points in the spatiotemporal domain over which the residual of the PDE is minimized. N_{Γ_u} and N_{Γ_t} represent the number of training points on boundaries, specifying Dirichlet and Neumann boundary conditions for displacements respectively, while N_{Γ_p} and N_{Γ_q} denote the corresponding number of training points for pressures on the boundaries. $N_{\Gamma_{IC}}$ and $N_{\Gamma_{int}}$ denote the number of training points on the initial condition and interface respectively. λ_i represents the corresponding relative weight (penalty) for each loss term MSE_i with respect to the weight for the loss term of the governing PDEs. Also, \odot implies the boundary or initial values for each corresponding term. The DNN approximates the output fields \tilde{u} and \tilde{p} . Points in the spatiotemporal domain are extracted through biased sampling, where the density decreases over time, as illustrated in Figure 5(b). The biased sampling approach is to be contrasted with structured sampling shown in Figure 5(a). The biased sampling approach prioritizes early-time solutions in accordance with causality and therefore, yields significantly improved results compared to the structured sampling approach [44]. Additionally, points were randomly sampled while retaining the bias, in contrast to the structured grid sampling. For brevity, only the results obtained from the neural networks utilizing training points obtained through a biased sampling approach are presented.

The optimal set of parameters for all experiments outlined in this paper is obtained using the Adam optimization algorithm [45] with an initial learning rate of 10^{-3} . Training is conducted using the functions provided by the JAX library [46], a robust numerical computing library designed for high-performance machine learning research. The computations are executed on the NVIDIA T4 GPU, which is accessible through the Google Colaboratory platform [47].

3.4. Glorot Initialization and Hard Enforcement of Boundary/initial Conditions

In recent years, various strategies have been explored to enhance the performance of PINNs in solving PDEs [48, 49, 50]. These efforts often involve

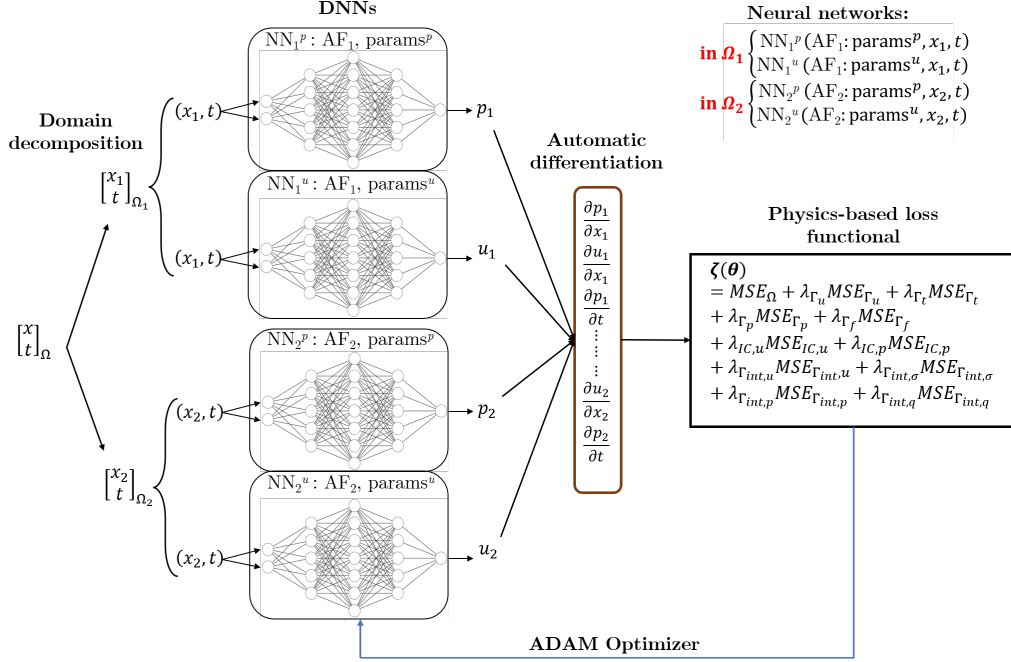


Figure 3: I-PINNs for 1-D coupled poroelasticity with an interface using a composite neural network (CoNN) architecture. Networks NN_1^p and NN_2^p model pressures across Ω_1 and Ω_2 with identical parameters (params^p) but distinct activation functions (AF_1 and AF_2), while NN_1^u and NN_2^u model displacements across Ω_1 and Ω_2 with shared parameters (params^u) and different activation functions (AF_1 and AF_2). In a nutshell: across subdomains, activation functions vary; between fields, only parameters differ.

designing more effective neural network architectures or improving training algorithms, incorporating techniques such as proper non-dimensionalization of equations, efficient sampling methods, the use of adaptive activation functions, and positional embeddings, among others. In this study, the two benchmark problems are initially solved using the proposed CoNN framework in its vanilla form. Subsequently, two special modifications are applied: Glorot initialization and hard enforcement of boundary and initial conditions (B/ICs). Detailed descriptions of these modifications are provided in the subsections that follow.

3.4.1. Glorot initialization

Before the commencement of training, the parameters of our DNN undergo initialization through a normally distributed random variable, with a

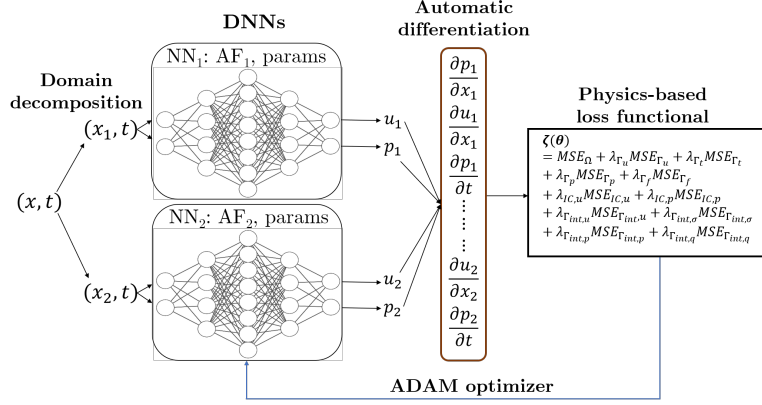


Figure 4: I-PINNs architecture for 1-D coupled poroelasticity with an interface using a single neural network (SNN) for each subdomain (NN_1 and NN_2 for Ω_1 and Ω_2 respectively). Each neural network outputs two field variables (pressures and displacements) for their respective sub-domains. These neural networks share the same set of parameters ‘params’ but use different activation functions AF_1 and AF_2 (in accordance to I-PINNs).

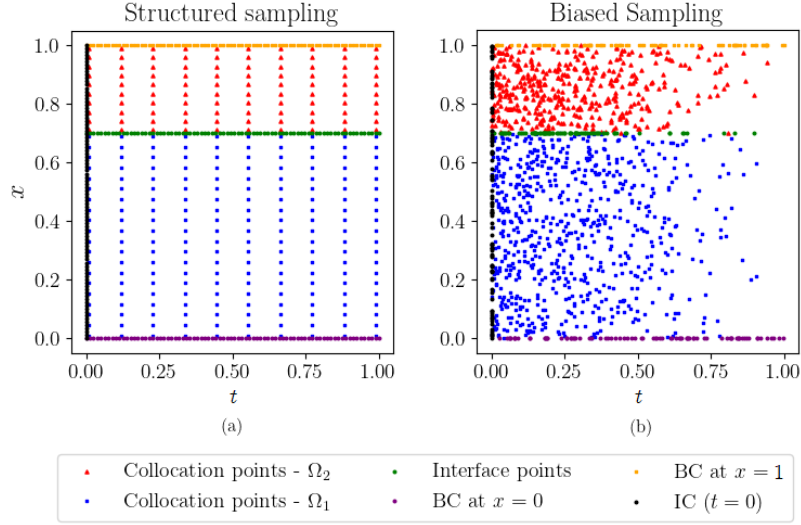


Figure 5: Representative figure where training points are sampled from – inside the two sub-domains (collocation points in Ω_1 and Ω_2), on the two boundaries (BC at $x = 0$ and $x = 1$) and at the initial condition (IC at $t = 0$), using two sampling techniques: (a) in a structured grid, (b) in a biased manner.

mean of zero and a standard deviation specified by a scaling factor (set to 0.1). This random initialization is applied to both the weight matrices and

bias vectors of each layer in the neural network. However, this initialization is found to play a crucial role in the effectiveness of gradient descent algorithms. The Glorot initialization scheme [51] is followed to improve the performance of the method. The scheme involves initializing the weights of a neural network layer by drawing random values from a distribution with a mean of 0 and a variance calculated as $\frac{2}{n_{\text{in}}+n_{\text{out}}}$, where n_{in} is the number of input units, and n_{out} is the number of output units in the layer. The biases are set to zero. The Glorot initialization helps prevent issues such as vanishing or exploding gradients during training by appropriately scaling the weights, thereby promoting stable and efficient convergence in deep learning models.

3.4.2. Hard enforcement of boundary/initial conditions

In the context of PINNs, the conventional approach to applying B/ICs is to penalize the discrepancy of initial and boundary constraints for PDEs in a “soft manner.” Alternatively, a more robust strategy is to enforce these conditions in a “hard” manner by incorporating specific solutions that rigorously satisfy the B/ICs [52, 53, 54]. This augmentation significantly enhances the neural networks’ capability to grapple with intricate geometric challenges.

When the initial condition (IC) is “soft-enforced,” the deep neural network $\mathcal{N}(x, t, \theta)$ approximates the function $u(x, t)$ as $u(x, t) \approx \tilde{u}(x, t) = \mathcal{N}(x, t, \theta)$ with the initial condition of $u_0(x)$ at $t = 0$. Conversely, in the case of “hard enforcement,” a new function \tilde{u} is created to approximate $u(x, t)$ while satisfying the initial condition for all $\mathcal{N}(x, t, \theta)$, given by:

$$\tilde{u}(x, t) = u_0(x) + t\mathcal{N}(x, t, \theta).$$

For the “hard-enforcement” of the Dirichlet boundary condition, where u_{D1} is imposed at $x = x_{\text{min}}$ and u_{D2} at $x = x_{\text{max}}$, a function \tilde{u} is created to approximate $u(x, t)$ as follows,

$$\tilde{u}(x, t) = (x - x_{\text{min}})(x - x_{\text{max}})\mathcal{N}(x, t, \theta) - u_{D1}\frac{x - x_{\text{max}}}{x_{\text{max}} - x_{\text{min}}} + u_{D2}\frac{x - x_{\text{min}}}{x_{\text{max}} - x_{\text{min}}}.$$

In both scenarios, there is no explicit need to specify the B/ICs in the loss functional, as the function $\tilde{u}(x, t)$ is meticulously crafted to automatically adhere to the relevant B/ICs.

4. Numerical Experiments

In this section, the performance of the two proposed frameworks, namely, I-PINNs with CoNN and I-PINNs with SNN, is compared with each other, as well as with conventional PINNs. This comparison is conducted on two benchmark examples examining poroelasticity in heterogeneous materials with a single interface. In Section 4.4, a comparative analysis is presented by solving the same benchmark problems with and without Glorot initialization and hard enforcement of B/ICs. To rigorously evaluate the accuracy of the proposed framework in addressing poroelastic problems, it's imperative to compare the approximations with closed-form analytical solutions. Although such solutions are scarce for heterogeneous poroelastic scenarios, a few have been found for 1D problems [55]. The results of this study were directly compared with the exact solutions provided in this literature. All pertinent details, including the problem domain, interface location, material properties, and the closed-form analytical solutions for both problems, are extracted from Bean and Yi [55].

It is important to note that while the exact solutions conform to the boundary conditions (Eqs. (6a) and (6b)), they no longer satisfy the initial condition (Eq. (6c)). The initial condition is determined by evaluating the given exact solutions at $t = 0$. For conciseness, the collectively proposed methods are referred to as I-PINNs (CoNN and SNN), while the conventional PINNs method is denoted simply as PINNs. The comparisons are based on two key factors: computational cost (total time for training the models) and accuracy, measured by the root mean square error against the closed-form analytical solution. Furthermore, both frameworks are enhanced with various modifications, as described in the previous section, and the impact of each modification on the accuracy of approximations is assessed. Finally, the convergence profiles of the CoNN and SNN models for the test cases are investigated.

Firstly, certain standards, such as the neural network architecture, total number of iterations, parameter scale for initialization, etc., must be established to ensure consistent comparisons. To determine these standards, we begin by considering a 1D homogeneous problem involving a compressible fluid. The material constants and the analytical solution for this problem are provided below -

$$\nu = 1, \quad \kappa = 1, \quad a = 0.01. \tag{14}$$

$$\begin{aligned}
p(x, t) &= \cos\left(\frac{20}{3}\right) \sin(x) e^{-100t/101}, \\
u(x, t) &= -\cos\left(\frac{20}{3}\right) \cos(x) e^{-100t/101}.
\end{aligned}
\tag{15}$$

It is noteworthy that for this specific problem, the revised boundary conditions are derived from Eq. (15), given that the original boundary conditions (Eqs. (6a) and (6b)) are no longer applicable. In the CoNN framework, the hyperbolic-tangent (tanh) activation function is employed for training over 70,000 iterations with an initial learning rate of 10^{-3} , initializing parameters at a scale of 0.1. The training set includes 5200 points, comprising 4900 collocation points, 100 points on each boundary, and 100 points at the initial condition. The RMSE for each potential architecture is computed, considering combinations of 1, 2, 3, 4 hidden layers and 5, 10, 20, 40, 80 hidden neurons in each layer, resulting in a total of 20 possible architectures. The weight (penalty) on each loss term is kept as 1.

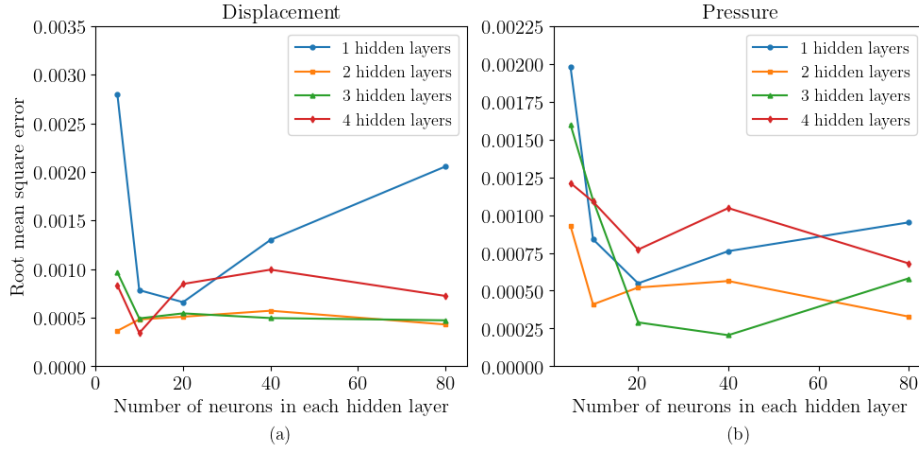


Figure 6: The plots illustrate the root mean square errors (RMSEs) corresponding to the approximations of displacements and pressure fields by our proposed I-PINNs with CoNN framework for the homogeneous compressible fluid problem. Various combinations of hidden layers (1,2,3,4) and neurons per layer (5,10,20,40,80) are examined, providing insights into the sensitivity of the model to different architectural configurations.

From Figure 6, it is evident that with a single layer and 5 hidden neurons, the RMSE is high for both displacement and pressure. As the number of neurons increases to 20, the root mean square error (RMSE) decreases, but further increments result in an upsurge. Analyzing the displacement

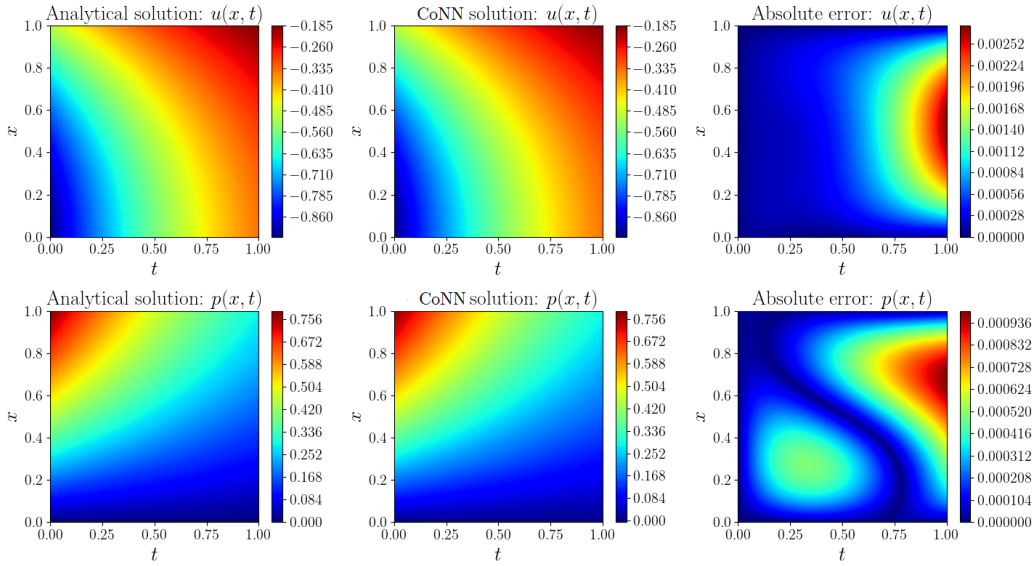


Figure 7: The displacements and pressure fields, accompanied by their respective absolute error contour plots, as approximated by the proposed I-PINNs with CoNN architecture for a homogeneous compressible fluid flow-problem. The activation functions GELU and tanh are employed across the two subdomains separated by the interface.

plot reveals that this issue is promptly addressed by incorporating multiple hidden layers. With multiple hidden layers, even using only 5 hidden neurons in each layer results in low RMSEs. However, for pressures, the task is more challenging, necessitating a higher number of neurons in each layer and more hidden layers to reduce the RMSE. Given that the aim is to deal with coupled poroelasticity problems, it is very important to choose a specific layer architecture that consistently results in relatively low errors in approximating both output fields – displacements and pressures. In this regard, while a 4 hidden layer architecture with 10 neurons each may yield a lower RMSE for displacements (as seen in Figure 6(a)), it performs poorly for the pressure field (indicated in Figure 6(b)). Therefore, it is essential to choose a layer architecture that minimizes the RMSE for both output fields rather than optimizing for just one. Considering both output fields, only two combinations – 3 layers with 40 neurons each and 2 hidden layers with 80 neurons each – meet this criterion. We opt for the former among the two as the standard layer architecture for all subsequent experiments due to its relative simplicity, respecting computational cost considerations. The approximated pressure and displacement plots, along with their corresponding

absolute error contour plots, are presented in Figure 7. For this simulation, we employed the aforementioned layer architecture consisting of 3 layers with 40 neurons each. It is evident that this specific layer architecture has effectively approximated both fields, with errors mostly lying close to $t = 1$ (near the characteristic time).

The discussion now transitions to two specific 1D heterogeneous problems, one featuring an incompressible fluid and the other involving a compressible fluid. The details for each are provided in the subsequent subsections.

4.1. Problem 1: Heterogeneous Poroelastic Media with an Incompressible Fluid

First, the problem described in Eqs. (4)-(5) is considered without any volumetric source/sink terms (i.e., $f_1(x, t) = f_2(x, t) = 0$) and with incompressible fluid in both subdomains (i.e., $a_1 = a_2 = 0$). The computational domain is considered as $x \in (0, 1), 0 \leq t \leq 1$, with a fixed material interface at $x = \zeta = 1/5$, that divides the problem domain into two non-overlapping subdomains, $x_1 \in (0, \zeta)$, and $x_2 \in (\zeta, 1)$. The elastic constants and the conductivities are specified as

$$\begin{aligned} \nu(x) &= \begin{cases} \nu_1 = 1, & x \leq \zeta \\ \nu_2 = \frac{\tan(1/15)\tan(12\pi/5)}{9\pi}, & x > \zeta \end{cases}, \\ a(x) &= \begin{cases} a_1 = 0, & x \leq \zeta \\ a_2 = 0, & x > \zeta \end{cases}, \\ \kappa(x) &= \begin{cases} \kappa_1 = 1, & x \leq \zeta \\ \kappa_2 = \frac{1}{\tan(1/15)\tan(12\pi/5)}, & x > \zeta \end{cases}. \end{aligned} \quad (16)$$

The displacements, tractions, pressures, and fluxes are assumed to be continuous at the interface as per Eq. (7). The analytical solutions for pressures and displacements for the problem are given below

$$\begin{aligned} p(x, t) &= \begin{cases} \cos\left(\frac{12\pi}{5}\right) \sin\left(\frac{x}{3}\right) e^{-t/9}, & x \leq \zeta \\ \sin\left(\frac{1}{15}\right) \cos(3\pi(1-x)) e^{-t/9}, & x > \zeta \end{cases}, \\ u(x, t) &= \begin{cases} -3 \cos\left(\frac{12\pi}{5}\right) \cos\left(\frac{x}{3}\right) e^{-t/9}, & x \leq \zeta \\ -\frac{3 \cos(1/15)}{\tan(12\pi/5)} 3 \sin(3\pi(1-x)) e^{-t/9}, & x > \zeta \end{cases}, \end{aligned} \quad (17)$$

Approximations to displacements and pressures in both sub-domains were constructed using both PINNs and I-PINNs (CoNN and SNN) for this model

problem using the hyperparameters detailed in Table 1. It was observed that when using identical hyperparameters, I-PINNs with CoNN achieved an RMSE of $\mathcal{O}(10^{-4})$ for both displacements and pressures, while I-PINNs with SNN achieved an RMSE of $\mathcal{O}(10^{-3})$, which is one order lower. However, conventional PINNs were only able to obtain RMSE of $\mathcal{O}(10^{-2})$. It is also interesting to observe that although I-PINNs with CoNN use almost twice the number of parameters than that of I-PINNs with SNN, the computation time taken by the latter is marginally higher (by 9%) than the former.

Table 1: Hyper-parameters used in training both PINNs & I-PINNs (CoNN and SNN) models for approximating the solution to the incompressible fluid problem. The activation functions are hyperbolic-tangent (tanh) and Gaussian error linear unit (GELU).

Parameter	I-PINNs (CoNN)	I-PINNs (SNN)	PINNs
Layer architecture	[2,40,40,40,1] \times 2	[2,40,40,40,2]	[2,40,40,40,1] \times 2
Activation functions	GELU-tanh	GELU-tanh	GELU
Number of training points [domain interior, external boundaries, interface]	[4900,140,70]	[4900,200,100]	[4900,200,100]
Penalty [interface condi- tions, boundary condi- tions, initial condition]	[200, 500, 300]	[200, 500, 300]	[200, 500, 300]
Maximum iterations	70000	70000	70000
RMSE (displacements)	2.6×10^{-4}	3.7×10^{-3}	5.4×10^{-2}
RMSE (pressures)	4.2×10^{-4}	4.8×10^{-3}	4.0×10^{-2}
Training time	631 seconds	706 seconds	465 seconds

The results (for both displacements and pressures) and the corresponding absolute errors obtained from both the I-PINNs frameworks (SNN and CoNN) as well as PINNs are shown in Figs. 8 and 9, respectively. Note that the maximum error occurs near the interface for PINNs. This is expected since the material property mismatch results in discontinuous gradients for pressures and displacements at the interface, and PINNs struggle to approximate these weak discontinuities accurately. Among the two I-PINNs models, the CoNN model approximated the fields with lesser errors compared to that of SNN. The maximum error in SNN is at least twice that of CoNN for both the displacement and pressure fields.

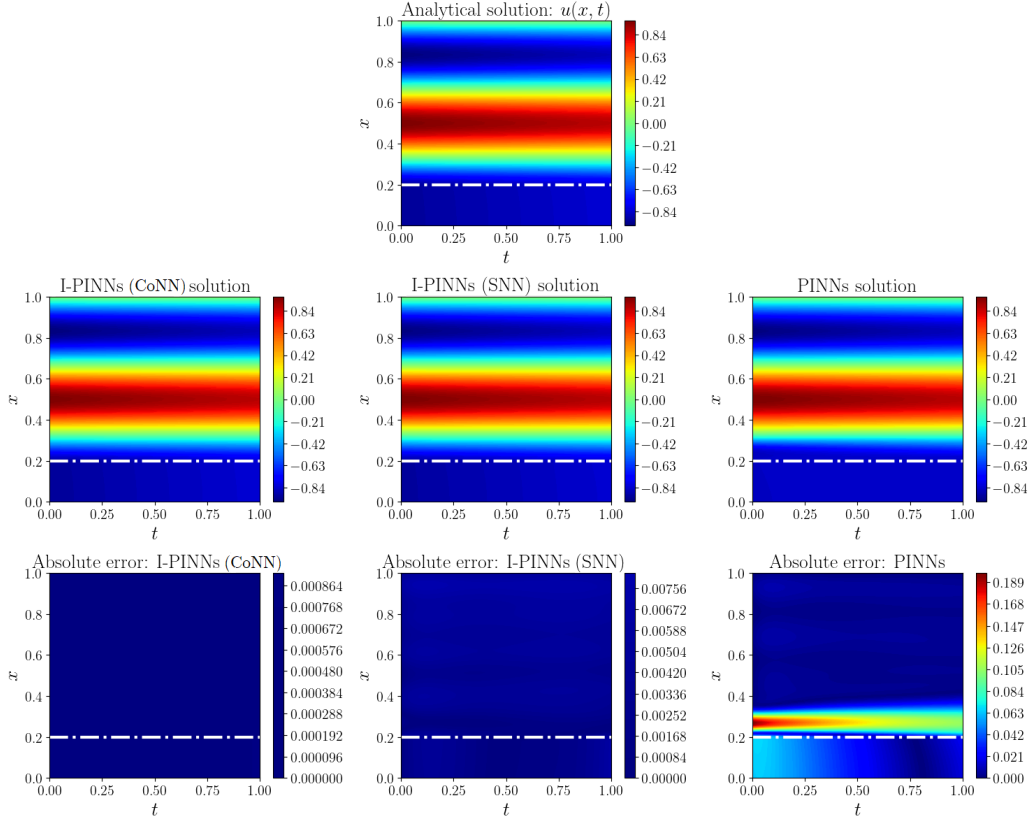


Figure 8: Displacement fields obtained by the two I-PINNs frameworks – SNN and CoNN, and as well as conventional PINNs (second row) for the incompressible fluid problem ($a = 0$). The third row displays the corresponding absolute errors. The interface (at $x = \zeta = 1/5$) is demarcated with a white dash-dot line.

4.2. Problem 2: Heterogeneous Poroelastic Media with a Compressible Fluid

As a second test problem, the problem described in Section 4.1 is modified by relaxing the assumption of fluid incompressibility. The problem domain remains identical, but the interface is now at $x = \zeta = 1/3$. The new material coefficients and the subsequent analytical solutions for pressures and displacements are listed below:

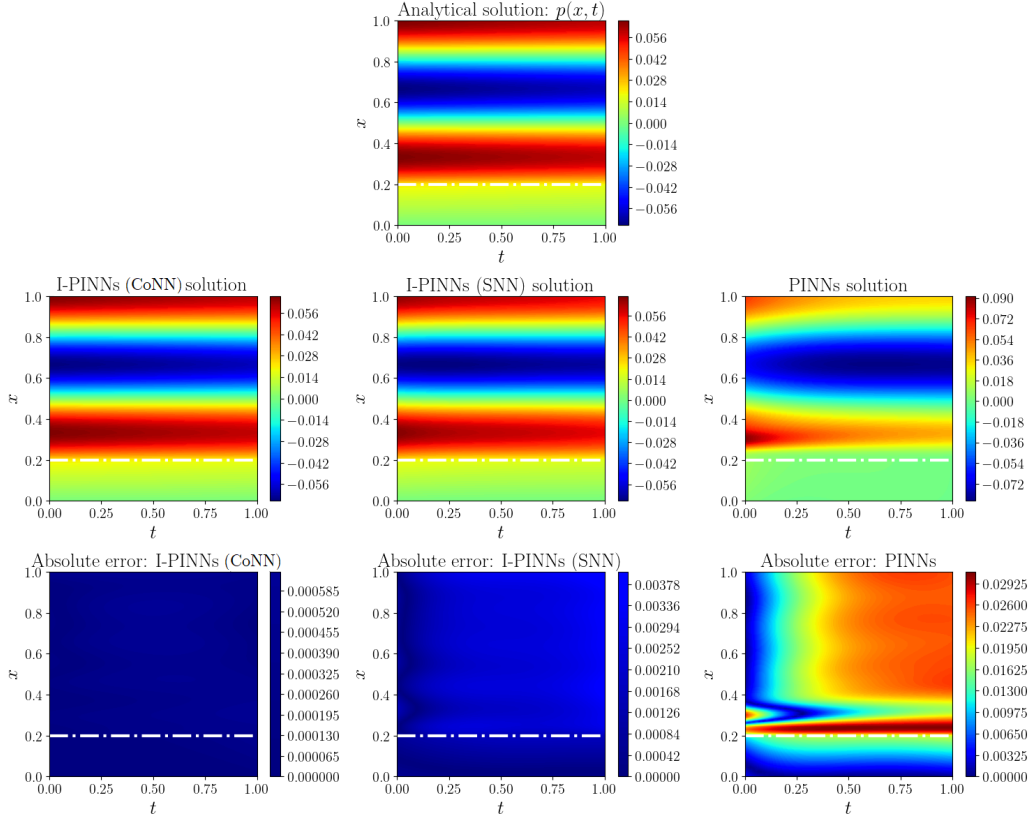


Figure 9: Pressure fields obtained by the two I-PINNs frameworks – SNN and CoNN, and as well as conventional PINNs (second row) for the incompressible fluid problem ($a = 0$). The third row displays the corresponding absolute errors. The interface (at $x = \zeta = 1/5$) is demarcated with a white dash-dot line.

$$\begin{aligned}
 \nu(x) &= \begin{cases} \nu_1 = 1, & x \leq \zeta \\ \nu_2 = \frac{\tan(1/3) \tan(20/3)}{10}, & x > \zeta \end{cases}, \\
 a(x) &= \begin{cases} a_1 = 0.01, & x \leq \zeta \\ a_2 = \frac{1}{10 \tan(1/3) \tan(20/3)}, & x > \zeta \end{cases}, \\
 \kappa(x) &= \begin{cases} \kappa_1 = 1, & x \leq \zeta \\ \kappa_2 = \frac{1}{10 \tan(1/3) \tan(20/3)}, & x > \zeta \end{cases}.
 \end{aligned} \tag{18}$$

$$\begin{aligned}
p(x, t) &= \begin{cases} \cos\left(\frac{20}{3}\right) \sin\left(\frac{x}{3}\right) e^{-100t/101}, & x \leq \zeta \\ \sin\left(\frac{1}{3}\right) \cos(10(1-x)) e^{-100t/101}, & x > \zeta \end{cases}, \\
u(x, t) &= \begin{cases} -3 \cos\left(\frac{20}{3}\right) \cos(x) e^{-100t/101}, & x \leq \zeta \\ -\frac{\sin(1/3) \sin(10(1-x))}{\tan(1/3) \tan(20/3)} e^{-100t/101}, & x > \zeta \end{cases},
\end{aligned} \tag{19}$$

Once again, the performance of the two I-PINNs frameworks is compared with each other, as well as with PINNs using a relatively simple architecture with identical hyperparameters for the three, as listed in Table 2. It is interesting to note that, in this case, both I-PINNs with CoNN and I-PINNs with SNN approximates the solution with an RMSE of $\mathcal{O}(10^{-3})$ for both displacements and pressures. Conversely, PINNs struggle to capture the heterogeneous response, resulting in substantially higher RMSEs of $\mathcal{O}(10^0)$ and $\mathcal{O}(10^{-1})$ for the two fields, respectively. Once again, it is noted that despite having fewer parameters, SNN requires more computation time (higher by 5%) than CoNN.

Table 2: Hyper-parameters used in training both PINNs & I-PINNs (CoNN and SNN) models for approximating the solution to the compressible fluid problem. The activation functions are hyperbolic-tangent (tanh) and Gaussian error linear unit (GELU).

Parameter	I-PINNs (CoNN)	I-PINNs (SNN)	PINNs
Layer architecture	[2,40,40,40,1] × 2	[2,40,40,40,2]	[2,40,40,40,1] × 2
Activation functions	GELU-tanh	GELU-tanh	GELU
Number of training points [domain interior, external boundaries, interface]	[4900,140,70]	[4900,200,100]	[4900,200,100]
Penalty [interface condi- tions, boundary condi- tions, initial condition]	[200, 500, 300]	[200, 500, 300]	[200, 500, 300]
Maximum iterations	70000	70000	70000
RMSE (displacements)	5.7×10^{-3}	7.6×10^{-3}	1.9×10^0
RMSE (pressures)	4.5×10^{-3}	3.3×10^{-3}	3.0×10^{-1}
Training time	718 seconds	754 seconds	487 seconds

Unlike the incompressible fluid case, here, the temporal derivative of pressure does not vanish ($\frac{\partial p}{\partial t} \neq 0$ as $a \neq 0$). Therefore, displacements and pressures both exhibit strong transient characteristics due to their high coupling. The results for both displacements and pressures obtained from I-PINNs and PINNs are depicted in Figs. 10 and 11. Notably, in this case, rather

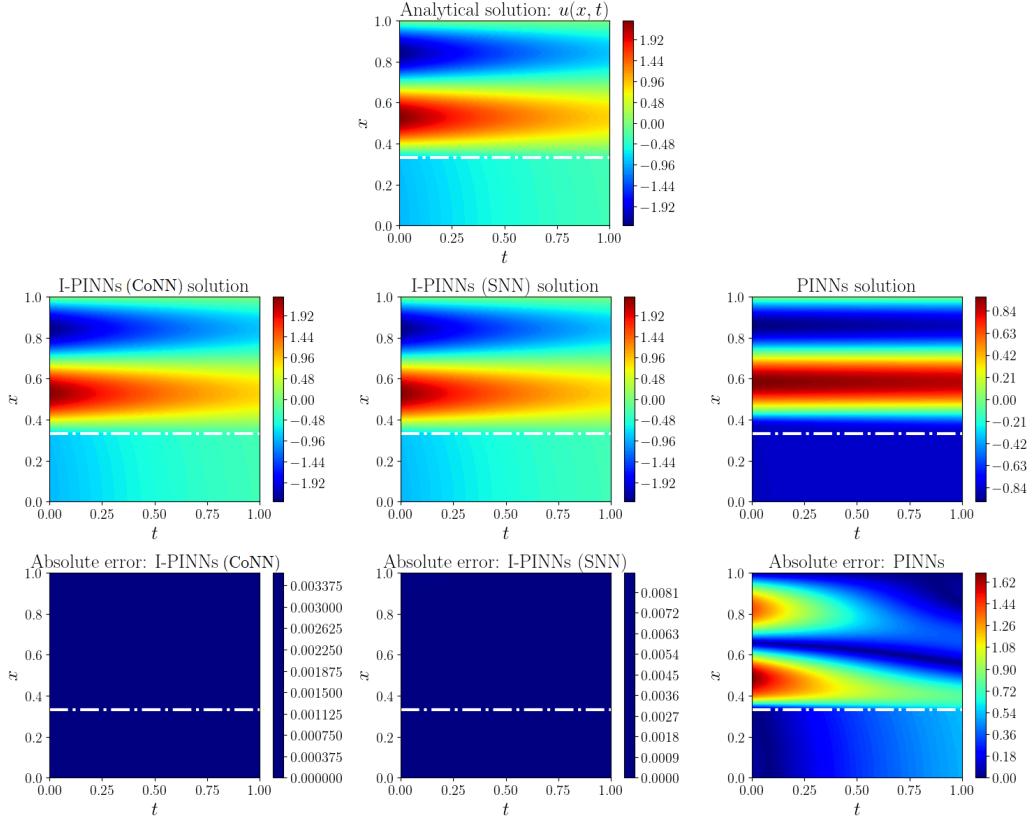


Figure 10: Displacement fields obtained by the two I-PINNs frameworks – SNN and CoNN, and as well as conventional PINNs (second row) for the compressible fluid problem ($a \neq 0$). The third row displays the corresponding absolute errors. The interface (at $x = \zeta = 1/3$) is demarcated with a white dash-dot line.

than accumulating predominantly near the interface, the error is dispersed throughout the entire domain, particularly pronounced in Ω_2 . This error distribution signifies an inadequate approximation across the entire domain and demonstrates the limitations of conventional PINNs for transient poroelasticity in heterogeneous materials. Both the I-PINNs frameworks approximate the output fields well, with errors consistently falling within the same order of magnitude, i.e., $\mathcal{O}(10^{-3})$. Further insights from Figs. 10 and 11 reveal that, although the maximum error in displacements approximated by SNN is slightly higher than that of CoNN, the reverse is true for approximations in pressures, but this difference is very minor and negligible. This leads to the conclusion that, while for an incompressible fluid problem I-PINNs with

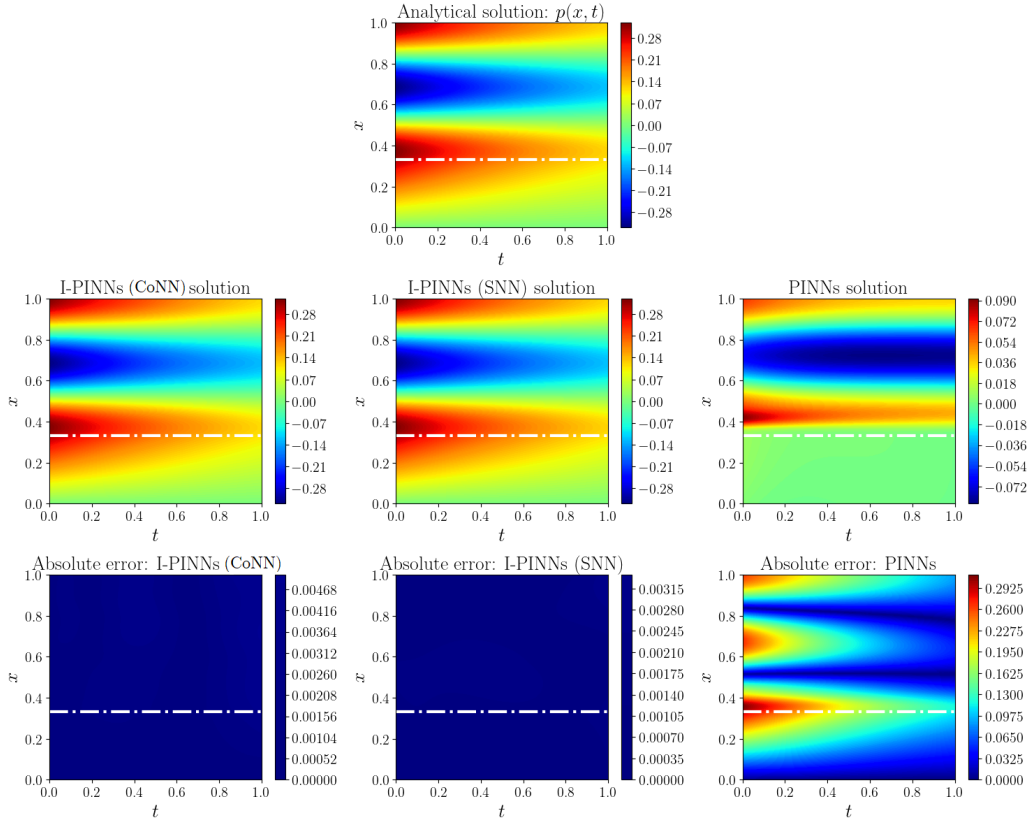


Figure 11: Pressure fields obtained by the two I-PINNs frameworks – SNN and CoNN, and as well as conventional PINNs (second row) for the compressible fluid problem ($a \neq 0$). The third row displays the corresponding absolute errors. The interface (at $x = \zeta = 1/3$) is demarcated with a white dash-dot line.

CoNN outperforms I-PINNs with SNN, for a compressible fluid problem, they largely display the same level of accuracy in approximations. In the next section, the convergence profiles of the two frameworks are compared, and further insights into their performance are drawn.

4.3. Convergence Behaviour

Examining the convergence profiles in Figure 12 for the two problems addressed by the I-PINNs frameworks, distinct observations emerge. In the context of the incompressible fluid problem, both frameworks—whether utilizing CoNN or an SNN—display a comparable level of oscillations during convergence. However, a notable difference is observed in the objective func-

tion values at each iteration, with CoNN consistently yielding significantly lower values than SNN. For the compressible fluid test case discussed in Section 4.2, the convergence profile for SNN exhibits noticeably higher oscillations compared to CoNN. This disparity highlights differing convergence dynamics between the two architectures, with CoNN demonstrating better convergence behavior for both test cases.

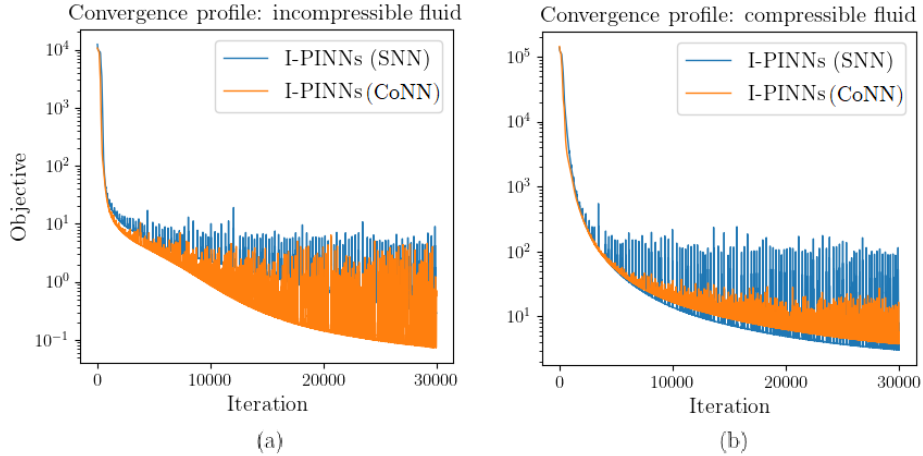


Figure 12: Convergence profiles depicting the optimization process for two experiments: (a) incompressible fluid and (b) compressible fluid. The plots display the objective function against iteration count for two models—I-PINNs with single neural network (SNN) and I-PINNs with composite neural network (CoNN).

4.4. Improvements on the Framework

Now, the I-PINNs (CoNN) framework is enhanced with the modifications outlined in section 3.3 (Glorot initialization, hard enforcement of boundary and initial conditions). The layer architecture is maintained consistently with the experiments in the previous sections (4 hidden layers with 40 neurons each), trained for 70,000 iterations. When hard enforcing the initial and boundary conditions, it is important to note that the number of points required for training decreases depending on which constraint is being hard enforced. Table 3 presents the RMSE when each of the modifications is applied to the vanilla version of our framework.

Right from the outset, it is evident that the hard enforcement of boundary and initial conditions significantly improves the accuracy of the approximations. This improvement is particularly pronounced for the compressible

fluid case, where enforcing these conditions effectively reduces the RMSE from $\mathcal{O}(10^{-3})$ to $\mathcal{O}(10^{-4})$ for both displacements and pressures. In the incompressible fluid scenario, a similar substantial improvement in pressures is observed, with both hard enforcement of initial conditions and boundary conditions resulting in a one-order-of-magnitude reduction in RMSE. However, for displacements, the significant decrease in RMSE from $\mathcal{O}(10^{-3})$ to $\mathcal{O}(10^{-4})$ is exclusively attributed to the hard enforcement of initial conditions while the impact of hard enforcement of boundary conditions remains negligible. The Glorot scheme for initializing network parameters (weights and biases) does contribute to improvements in the approximations, albeit marginally. While the order of magnitude remains consistent, there is a subtle reduction in magnitude.

Table 3: Performance comparison of the proposed I-PINNs with CoNN architectures with various modifications for the incompressible and compressible fluid flow problems. The accuracy is measured using the root mean square error (RMSE) metric.

	I-PINNs (CoNN)	+ Glorot initialization	+ Hard BC	+ Hard IC
Incompressible (displacements)	2.6×10^{-4}	1.5×10^{-4}	1.1×10^{-4}	5.6×10^{-5}
Incompressible (pressures)	4.2×10^{-4}	3.5×10^{-4}	9.6×10^{-5}	3.1×10^{-5}
Compressible (displacements)	5.7×10^{-3}	2.2×10^{-3}	7.6×10^{-4}	5.1×10^{-4}
Compressible (pressures)	4.5×10^{-3}	3.7×10^{-3}	8.3×10^{-4}	6.5×10^{-4}

5. Conclusions

In this study, a novel Physics-Informed Neural Networks (PINNs) framework was introduced for modeling coupled problems specifically tailored for thermo-hydro-poromechanical systems in heterogeneous subsurface media. Notably, the framework’s application was limited to heterogeneous poroelastic media for this study, and the results showcased superior accuracy and convergence compared to the conventional PINNs framework. The approach incorporated two significant modifications to the neural network architecture. Firstly, a composite neural network (CoNN) was employed, where each sub-domain featured a dedicated neural network for each output field variable (displacements and pressures). These neural networks utilized the same

activation functions but were trained separately for their network parameters (weights and biases). Secondly, the neural network was integrated into the Interface-PINNs (I-PINNs) framework, employing different activation functions across material interfaces to capture discontinuities in solution fields and gradients accurately. Collocation points for training the I-PINNs were prescribed using a biased sampling approach, prioritizing early-time solutions in accordance with causality. Additional modifications were introduced into the proposed framework, including initializing the network parameters using the Glorot scheme and hard enforcing the initial and boundary conditions. The accuracy and convergence behavior of the proposed framework was demonstrated through two specific numerical examples involving an incompressible fluid and a compressible fluid. A single neural network (SNN) architecture was also explored, integrated into the I-PINNs framework, and compared against the proposed CoNN. In comparison to the conventional PINNs framework, both proposed I-PINNs frameworks (CoNN and SNN) exhibited superior accuracy in benchmark numerical examples. While I-PINNs with SNN showed improved results over conventional PINNs, the standout performer was I-PINNs with CoNN, demonstrating better convergence behavior and improved accuracy, especially in the incompressible fluid example. Moreover, the training times for I-PINNs with SNN were slightly higher than those of I-PINNs with CoNN, making them computationally costlier. Moreover, it is essential to highlight the framework’s potential for extension to include thermo-mechanical aspects, which were not explicitly addressed in the current study. Looking ahead, future work involves expanding the proposed approach to address two-dimensional and three-dimensional poroelastic problems and further enhance its capabilities to model coupled multiphysics processes, including thermo-hydro-poromechanical problems involving composite materials or highly heterogeneous subsurface systems.

Acknowledgement

Pratanu Roy’s work was performed under the auspices of the U.S. Department of Energy by Lawrence Livermore National Laboratory under Contract DE-AC52-07NA27344. Chandrasekhar Annavarapu gratefully acknowledges the support from ExxonMobil Corporation to the Subsurface Mechanics and Geo-Energy Laboratory under the grant SP22230020CEEXXU008957. The support from the Ministry of Education, Government of India and IIT

Madras under the grant SB20210856CEMHRD008957 is also gratefully acknowledged.

References

- [1] C. R. Fielding, R. C. Crane, An application of statistical modelling to the prediction of hydrocarbon recovery factors in fluvial reservoir sequences (1987).
- [2] J. P. Morris, W. W. McNab, S. K. Carroll, Y. Hao, W. Foxall, J. L. Wagoner, Injection and reservoir hazard management: the role of injection-induced mechanical deformation and geochemical alteration at in salah co2 storage project: status report quarter end, june 2009, in: LLNL Technical Report, 2009.
- [3] M. Bloemendal, T. Olsthoorn, F. Boons, How to achieve optimal and sustainable use of the subsurface for aquifer thermal energy storage, *Energy Policy* 66 (2014) 104–114.
- [4] A. Settari, F. Mounts, A coupled reservoir and geomechanical simulation system, *Spe Journal* 3 (03) (1998) 219–226.
- [5] A. Menin, V. A. Salomoni, R. Santagiuliana, L. Simoni, A. Gens, B. A. Schrefler, A mechanism contributing to subsidence above gas reservoirs and its application to a case study, *International Journal for Computational Methods in Engineering Science and Mechanics* 9 (5) (2008) 270–287.
- [6] B. Lecampion, A. Bungler, X. Zhang, Numerical methods for hydraulic fracture propagation: A review of recent trends, *Journal of natural gas science and engineering* 49 (2018) 66–83.
- [7] D. Ammosov, M. Vasilyeva, E. T. Chung, Generalized multiscale finite element method for thermoporoelasticity problems in heterogeneous and fractured media, *Journal of Computational and Applied Mathematics* 407 (2022) 113995.
- [8] J.-L. Adia, J. Yvonnet, Q.-C. He, N. Tran, J. Sanahuja, A combined lattice-boltzmann-finite element approach to modeling unsaturated poroelastic behavior of heterogeneous media, *Journal of Computational Physics* 437 (2021) 110334.

- [9] R. R. Settghost, P. Fu, S. D. Walsh, J. A. White, C. Annavarapu, F. J. Ryerson, A fully coupled method for massively parallel simulation of hydraulically driven fractures in 3-dimensions, *International Journal for Numerical and Analytical Methods in Geomechanics* 41 (5) (2017) 627–653. doi:<https://doi.org/10.1002/nag.2557>.
- [10] C. A. Srinivas, D. M. Valiveti, V. Dyadechko, Model for coupled porous flow and geomechanics for subsurface simulation, uS Patent App. 17/011,254 (Apr. 1 2021).
- [11] I. Sokolova, M. G. Bastisya, H. Hajibeygi, Multiscale finite volume method for finite-volume-based simulation of poroelasticity, *Journal of Computational Physics* 379 (2019) 309–324.
- [12] Q. A. Ahmad, M. I. Ehsan, N. Khan, A. Majeed, A. Zeeshan, R. Ahmad, F. M. Noori, Numerical simulation and modeling of a poroelastic media for detection and discrimination of geo-fluids using finite difference method, *Alexandria Engineering Journal* 61 (5) (2022) 3447–3462.
- [13] D. M. Valiveti, C. A. Srinivas, V. Dyadechko, Grid modification during simulated fracture propagation, US Patent No. 11,608,730 (Mar. 21 2023).
- [14] C. Annavarapu, An efficient finite element method for interface problems, Ph.D. thesis, Duke University (2013).
- [15] C. Annavarapu, M. Hautefeuille, J. Dolbow, A robust nitsche’s formulation for interface problems, *Computer Methods in Applied Mechanics and Engineering* 225-228 (2012) 44–54.
- [16] M. Raissi, P. Perdikaris, G. E. Karniadakis, Physics-informed neural networks: A deep learning framework for solving forward and inverse problems involving nonlinear partial differential equations, *Journal of Computational physics* 378 (2019) 686–707.
- [17] E. Haghighat, M. Raissi, A. Moure, H. Gomez, R. Juanes, A physics-informed deep learning framework for inversion and surrogate modeling in solid mechanics, *Computer Methods in Applied Mechanics and Engineering* 379 (2021) 113741.

- [18] E. Zhang, M. Dao, G. E. Karniadakis, S. Suresh, Analyses of internal structures and defects in materials using physics-informed neural networks, *Science advances* 8 (7) (2022) eabk0644.
- [19] S. Cai, Z. Mao, Z. Wang, M. Yin, G. E. Karniadakis, Physics-informed neural networks (pinns) for fluid mechanics: A review, *Acta Mechanica Sinica* 37 (12) (2021) 1727–1738.
- [20] H. Wessels, C. Weißenfels, P. Wriggers, The neural particle method—an updated lagrangian physics informed neural network for computational fluid dynamics, *Computer Methods in Applied Mechanics and Engineering* 368 (2020) 113127.
- [21] S. Cai, Z. Wang, S. Wang, P. Perdikaris, G. E. Karniadakis, Physics-informed neural networks for heat transfer problems, *Journal of Heat Transfer* 143 (6) (2021) 060801.
- [22] D. Jalili, S. Jang, M. Jadidi, G. Giustini, A. Keshmiri, Y. Mahmoudi, Physics-informed neural networks for heat transfer prediction in two-phase flows, *International Journal of Heat and Mass Transfer* 221 (2024) 125089.
- [23] D. R. Sarkar, C. Annavarapu, P. Roy, On the use of physics-informed neural networks to solve inverse problems in heterogeneous materials.
- [24] Y. Chen, L. Lu, G. E. Karniadakis, L. Dal Negro, Physics-informed neural networks for inverse problems in nano-optics and metamaterials, *Optics express* 28 (8) (2020) 11618–11633.
- [25] E. Haghighat, D. Amini, R. Juanes, Physics-informed neural network simulation of multiphase poroelasticity using stress-split sequential training, *Computer Methods in Applied Mechanics and Engineering* 397 (2022) 115141.
- [26] D. Amini, E. Haghighat, R. Juanes, Inverse modeling of nonisothermal multiphase poromechanics using physics-informed neural networks, *Journal of Computational Physics* 490 (2023) 112323.
- [27] O. Coussy, *Poromechanics*, John Wiley & Sons, 2004.

- [28] H.-s. Li, Z.-z. Lü, Z.-f. Yue, Support vector machine for structural reliability analysis, *Applied Mathematics and Mechanics* 27 (10) (2006) 1295–1303.
- [29] N. Ceryan, U. Okkan, P. Samui, S. Ceryan, Modeling of tensile strength of rocks materials based on support vector machines approaches, *International Journal for Numerical and Analytical Methods in Geomechanics* 37 (16) (2013) 2655–2670.
- [30] S. Joshi, S. K. Singh, S. Dubey, Machine learning and molecular dynamics based models to predict the temperature dependent elastic properties of silver nanowires, *International Journal for Computational Methods in Engineering Science and Mechanics* (2023) 1–9.
- [31] C. K. Williams, C. E. Rasmussen, Gaussian processes for machine learning, Vol. 2, MIT press Cambridge, MA, 2006.
- [32] A. Mujumdar, P. Robi, M. Malik, M. Horio, Artificial neural network (ann) model for prediction of mixing behavior of granular flows, *International Journal for Computational Methods in Engineering Science and Mechanics* 8 (3) (2007) 149–158.
- [33] F.-H. Hsiao, W.-L. Chiang, C.-W. Chen, Fuzzy control for nonlinear systems via neural-network-based approach, *International Journal for Computational Methods in Engineering Science and Mechanics* 6 (3) (2005) 145–152.
- [34] R. Al-Ajmi, H. Abou-Ziyan, M. Mahmoud, Performance evaluation of 14 neural network architectures used for predicting heat transfer characteristics of engine oils, *International Journal for Computational Methods in Engineering Science and Mechanics* 13 (1) (2012) 60–75.
- [35] G. Yagawa, H. Okuda, Neural networks in computational mechanics, *Archives of Computational Methods in Engineering* 3 (1996) 435–512.
- [36] L. B. Rall, *Automatic differentiation: Techniques and applications*, Springer, 1981.
- [37] R. R. Selmic, F. L. Lewis, Neural-network approximation of piecewise continuous functions: application to friction compensation, *IEEE transactions on neural networks* 13 (3) (2002) 745–751.

- [38] A. D. Jagtap, G. E. Karniadakis, Extended physics-informed neural networks (xpinns): A generalized space-time domain decomposition based deep learning framework for nonlinear partial differential equations., in: AAAI spring symposium: MLPS, Vol. 10, 2021.
- [39] A. K. Sarma, S. Roy, C. Annavarapu, P. Roy, S. Jagannathan, Interface pinns (i-pinns): A physics-informed neural networks framework for interface problems, *Computer Methods in Applied Mechanics and Engineering* 429 (2024) 117135.
- [40] A. Sarma, C. Annavarapu, P. Roy, S. Jagannathan, D. Valiveti, Variational interface physics informed neural networks (vi-pinns) for heterogeneous subsurface systems, in: *ARMA US Rock Mechanics/Geomechanics Symposium*, ARMA, 2023, pp. ARMA–2023.
- [41] B. Zhang, G. Wu, Y. Gu, X. Wang, F. Wang, Multi-domain physics-informed neural network for solving forward and inverse problems of steady-state heat conduction in multilayer media, *Physics of Fluids* 34 (11) (2022).
- [42] A. D. Jagtap, G. E. Karniadakis, Extended physics-informed neural networks (xpinns): A generalized space-time domain decomposition based deep learning framework for nonlinear partial differential equations, *Communications in Computational Physics* 28 (5) (2020).
- [43] S. Roy, C. Annavarapu, P. Roy, A. K. Sarma, Adaptive interface-pinns (adai-pinns): An efficient physics-informed neural networks framework for interface problems, *arXiv preprint arXiv:2406.04626* (2024).
- [44] J. Guo, H. Wang, C. Hou, A novel adaptive causal sampling method for physics-informed neural networks, *arXiv preprint arXiv:2210.12914* (2022).
- [45] D. P. Kingma, J. Ba, Adam: A method for stochastic optimization, *arXiv preprint arXiv:1412.6980* (2014).
- [46] J. Bradbury, R. Frostig, P. Hawkins, M. J. Johnson, C. Leary, D. Maclaurin, G. Necula, A. Paszke, J. VanderPlas, S. Wanderman-Milne, Q. Zhang, JAX: composable transformations of Python+NumPy programs (2018).
URL <http://github.com/google/jax>

- [47] E. Bisong, E. Bisong, Google colaboratory, Building machine learning and deep learning models on google cloud platform: a comprehensive guide for beginners (2019) 59–64.
- [48] P.-H. Chiu, J. C. Wong, C. Ooi, M. H. Dao, Y.-S. Ong, Can-pinn: A fast physics-informed neural network based on coupled-automatic–numerical differentiation method, *Computer Methods in Applied Mechanics and Engineering* 395 (2022) 114909.
- [49] P. Peng, J. Pan, H. Xu, X. Feng, Rpinns: Rectified-physics informed neural networks for solving stationary partial differential equations, *Computers & Fluids* 245 (2022) 105583.
- [50] S. Wang, S. Sankaran, H. Wang, P. Perdikaris, An expert’s guide to training physics-informed neural networks, *arXiv preprint arXiv:2308.08468* (2023).
- [51] X. Glorot, Y. Bengio, Understanding the difficulty of training deep feed-forward neural networks, in: *Proceedings of the thirteenth international conference on artificial intelligence and statistics, JMLR Workshop and Conference Proceedings*, 2010, pp. 249–256.
- [52] J. Deng, X. Li, J. Wu, S. Zhang, W. Li, Y.-G. Wang, Physical informed neural networks with soft and hard boundary constraints for solving advection-diffusion equations using fourier expansions, *arXiv preprint arXiv:2306.12749* (2023).
- [53] S. Berrone, C. Canuto, M. Pintore, N. Sukumar, Enforcing dirichlet boundary conditions in physics-informed neural networks and variational physics-informed neural networks, *arXiv preprint arXiv:2210.14795* (2022).
- [54] S. Liu, H. Zhongkai, C. Ying, H. Su, J. Zhu, Z. Cheng, A unified hard-constraint framework for solving geometrically complex pdes, *Advances in Neural Information Processing Systems* 35 (2022) 20287–20299.
- [55] M. Bean, S.-Y. Yi, An immersed interface method for a 1d poroelasticity problem with discontinuous coefficients, *Journal of computational and applied mathematics* 272 (2014) 81–96.